PAPER • OPEN ACCESS

High-fidelity simulations of wake-to-wake interaction in an atmospheric boundary layer over a complex terrain

To cite this article: C. Jané-Ippel *et al* 2023 *J. Phys.: Conf. Ser.* **2505** 012033

View the article online for updates and enhancements.

High-fidelity simulations of wake-to-wake interaction in an atmospheric boundary layer over a complex terrain

C. Jané-Ippel[1], N. Bempedelis[1], R. Palacios[1], S. Laizet[1]

[1]Imperial College London, Department of Aeronautics, London SW7 2AZ, UK

E-mail: `christian.jane-ippel19@imperial.ac.uk`, `n.bempedelis20@imperial.ac.uk`, `r.palacios@imperial.ac.uk`, `s.laizet@imperial.ac.uk`

Abstract. In this work, the wind farm simulator `WInc3D` is employed to perform large-eddy simulations (LES) of the flow over a complex terrain. The methodology used is validated through comparison with previously published wind tunnel experiments and numerical data for the flow over a cosine-squared hill with and without wind turbines. The study focuses on the wake-to-wake interaction between two wind turbines, with one on the hilltop and the other 2.5 or 5 turbine diameters downstream of the hilltop. The results indicate that the power output of the downstream turbine can be increased by a factor of three when a wind turbine is placed on the hilltop. This is explained by the accelerated flow that results from the favourable pressure gradient produced by the first half of the hill and the blockage of the hilltop turbine. It is also found that this effect is not sufficient to enhance the power of the downstream turbine if it is placed too far away from the upstream turbine.

1. Introduction

Wind energy is a major contributor to renewable energies and is essential for a sustainable future. The trend to reduce the cost and increase the efficiency of wind energy has been the use of larger wind turbines with blades that now reach over a hundred meters. At these length scales, an accurate representation of the dynamic interactions between the atmospheric boundary layer (ABL) and wind turbine wakes becomes essential for predicting wind farm power output and turbine loading [1,2]. Many onshore wind farms are likely to be situated on hilly terrain or close to urban centres, influencing the atmospheric boundary layer properties and wind turbine wakes. The complex terrain can induce wind speed-ups, veer, reverse flow and high levels of turbulence intensity affecting the resulting power output, loads and wake recovery of the turbines. Thus, accounting for the influence of the topography has proven to be crucial for optimal design and performance of wind farms [3,4].

In recent years, numerical studies on wind turbines in complex terrain have gained more interest due to the possibility of undertaking turbulence-resolving simulations, e.g. large-eddy simulations (LES), of the flow. Yang *et al.* [5] performed LES of the set-up presented by Howard *et al.* [6] where a wind turbine is placed in the wake induced by a 3D hill and showed good agreement with the experiments. Shamsoddin and Porté-Agel [7] showed a good agreement of their LES with the experimental study of Tian *et al.* [8], which includes flow measurements, power output and fatigue loads of an array of five wind turbines under the effect of a Gaussian

hill. Liu and Stevens [9] and Zhang *et al.* [10] validated their LES using an immersed boundary method (IBM) against the experimental results of the cosine-squared hill of Cao and Tamura [11]. The former studied the performance of a single wind turbine at different locations around the hill at different hub heights, the effects of having the hill in the middle of a wind farm and a wind farm located between two hills. The latter also studied the wind turbine performance around hills with two different slopes: a steep hill with flow separation and a gentle hill without separation.

In this work, we aim to validate our numerical methods by comparing our simulations to the experimental data of Cao and Tamura [11]. Furthermore, the computed power output of the wind turbines located at different positions around the hill will be compared against Liu and Stevens [9] and Zhang *et al.* [10]. Finally, new results are presented to discuss the influence of the hill and a wind turbine at the hilltop on a downwind turbine at two different streamwise locations downstream of the upstream turbine.

2. Numerical methods

The wind farm simulator used is `WInc3D` [12], an open source code that is part of the suite of flow solvers `Xcompact3D` [13]. The equations we solve are the unsteady, incompressible, filtered Navier-Stokes (N-S) equations with an explicit LES formulation,

$$\frac{\partial \widetilde{u}_i}{\partial t} + \frac{1}{2}\left(\widetilde{u}_j \frac{\partial \widetilde{u}_i}{\partial x_j} + \frac{\partial \widetilde{u}_i \widetilde{u}_j}{\partial x_j}\right) = -\frac{1}{\rho}\frac{\partial \widetilde{p}}{\partial x_i} - \frac{\partial \tau_{ij}}{\partial x_j} + \nu \frac{\partial^2 \widetilde{u}_i}{\partial x_j \partial x_j} + \frac{F_i}{\rho}, \tag{1}$$

$$\frac{\partial \widetilde{u}_i}{\partial x_i} = 0, \tag{2}$$

where $\widetilde{u}_i$ and $\widetilde{p}$ are the filtered components of velocity and pressure fields, ρ is the fluid density, τ_{ij} the subgrid-scale stresses, ν the kinematic viscosity and F_i the body forcing. It has to be noted that the viscous term is almost negligible due to the high-Reynolds number flows involved in the atmospheric boundary layer. The subfilter stresses are computed using the standard Smagorinsky model [14], that is $\tau_{ij} = -2\left(C_S \Delta\right)^2 |\widetilde{S}|\widetilde{S}_{ij}$, where C_s is the so-called Smagorinsky constant, Δ is the volumetric cell size and $\widetilde{S}_{ij}$ and $|\widetilde{S}|$ are the strain-rate tensor and its magnitude, respectively. The Smagorinsky constant is usually constant throughout the domain, but on atmospheric boundary layer simulations, a reduction to the Smagorinsky constant near the wall is necessary to avoid excessive dissipation at the surface [15–17]. To this end, we use the wall-damping function of Mason and Thomson [18] to correct the Smagorinsky constant as follows $C_S = \left(C_0^n + \left\{\kappa\left(\frac{y}{\Delta} + \frac{y_0}{\Delta}\right)\right\}^{-n}\right)^{-1/n}$, where $\kappa = 0.4$ is the von Kármán constant, y_0 is the roughness height of the boundary layer, C_0 is the far from wall Smagorinsky constant with value $C_0 = 0.14$, and n is the parameter that controls the growth from the wall with value $n = 3$. The framework uses a Cartesian mesh and compact finite-difference schemes for differentiating, filtering and interpolating. The spatial discretisation uses 6th-order schemes, and for the time advancement, an explicit 3rd-order Adams-Bashforth is used. The high-order compact finite difference schemes employed guarantee a "spectral-like" accuracy [19, 20] and allow the use of Dirichlet boundary conditions in the streamwise direction. The simplicity of a Cartesian mesh is exploited to use a 2D domain decomposition based on standardised MPI. The code has been proven to have excellent strong and weak scaling properties [21].

For the simulations of complex terrain and wind turbines in the atmospheric boundary layer, we use an inlet/outlet boundary condition. To provide the inflow atmospheric turbulence, we employ a precursor simulation of a neutrally stable atmospheric boundary layer with periodic boundary conditions for all lateral planes. A slip wall boundary condition is used on the top boundary, and a no-slip wall boundary condition is used on the bottom boundary. Due to the

high-Reynolds number flows in the ABL, and the relatively coarse mesh near the bottom wall, a wall model is used to capture the turbulent structures produced by the drag of the wall. The wall model employed is a wall-stress model that computes the stresses at the wall surface τ_w assuming an instantaneous log-law profile of a rough wall, such that $\tau_w = - \left[\frac{\kappa U_1}{\ln (y_1/y_0)} \right]^2$, where y_1 is the local height from the wall at which the velocity $U_1 = \sqrt{u_x^2 + u_z^2}$ is sampled in the fluid domain.

The body forcing F_i is used to drive the flow, to model the complex terrain with an IBM, and to model the wind turbines. In the precursor simulations, the flow is driven by a constant pressure gradient forcing in the streamwise direction equal to u_*^2/δ, where u_* is the friction velocity and δ is the boundary layer height. To include the terrain surface in the simulations with a Cartesian mesh, we use the IBM of Gautier *et al.* [22] and a modified version of the ABL wall model. Firstly, the method defines the nodes inside the solid domain so that the forcing term in the N-S equations (1) can be added. Then, the alternating direction forcing is applied in the solid domain to ensure a no-slip boundary condition on the fluid domain. This forcing consists of one-dimensional reconstructions of the solution inside the solid body to have better stability and remove the discontinuities at the wall of the immersed object. This forcing avoids staircase effects in the representation of the terrain surface so that the solution can be smooth and second-order accurate; refer to [22] for more details. This IBM has been used in several publications with both LES and DNS [23, 24], although it has to be noted this is the first time it is used together with a wall model. The wind turbines are parametrised with the actuator disk model (ADM) following the methodology presented by Calaf *et al.* [15], a porous disk with a uniform drag force on the volume of fluid contained within the swept area. The wind turbine thrust force acting on the flow is defined by $F_{wt} = -\frac{1}{2}\rho A_D \frac{C_T}{(1-a)^2}(u_d)^2$, where ρ is the fluid density, A_D is the rotor swept area, C_T the thrust coefficient, a is the rotor's induction factor and u_d disk-averaged and time-filtered velocity extracted from the fluid solver. The power of each wind turbine can be computed as $P_{wt} = -F_{wt}u_d$. This approach is computationally less expensive than the actuator line or the full rotor geometry simulation and has been widely used in the literature for utility-scale wind farms immersed in an atmospheric boundary layer [15, 25–28]. It is worth noting that the ADM has limitations, as it assumes a uniform flow through the disk, which does not represent real-world conditions. It does not account for three-dimensional effects caused by the rotation of the blades, the radial distribution of forces, or the effects of the nacelle and tower, all of which can significantly impact the near and far wake properties. However, for the purposes of this exploratory study, the ADM was deemed sufficient to assess the main trade-offs. While more advanced methods such as the actuator line or actuator surface models may provide a more accurate representation of the wind turbine wake, they are computationally expensive and not feasible with this study's current spatial and temporal resolution [29].

3. Validation
The complex terrain investigated in this work is a constant section hill studied experimentally by Cao and Tamura [11] described by

$$y_{hill}(x) = h \cos^2 \left(\frac{\pi x}{2L} \right), \qquad -L \leq x \leq L, \qquad (3)$$

where $h = 0.04\ m$ is the maximum height of the hill and $L = 0.1\ m$ is half-width of the hill. The incoming turbulence is defined by a turbulent boundary layer of height $\delta = 0.25\ m$, a friction velocity $u_* = 0.1926\ m/s$ and a roughness length $y_0 = 0.004\ mm$.

The computational domain has a size of $L_x \times L_y \times L_z = (5 \times 1 \times 1)\delta$. The actuator disk for the simulations with a wind turbine has a diameter of $D = h$, a thrust coefficient of $C_T = 0.75$ and an axial induction factor of $a = 0.25$ following the prior LES studies [9,10]. We place a wind turbine

at different streamwise locations around the hill: $x/D = -5.0, -2.5, -1.25, 0.0, 1.25, 2.5, 5.0$, where $x = 0$ is the centre of the hill. Figure 1 shows a schematic view of the computational domain with the hill and a wind turbine at the hilltop $x/D = 0.0$.
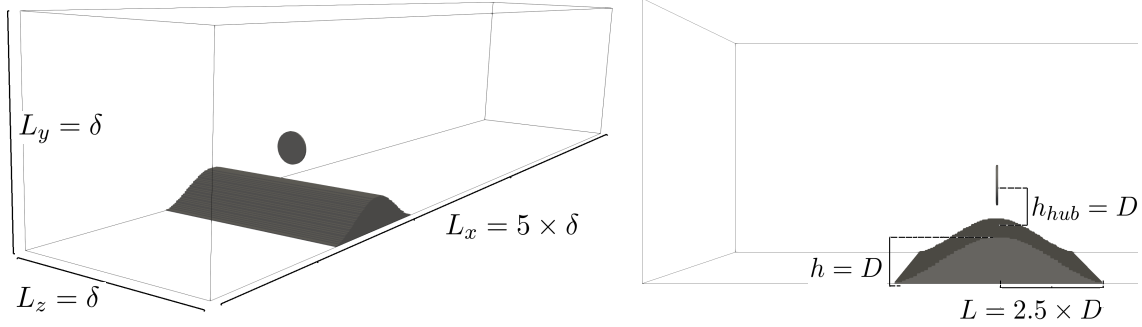

Figure 1: Schematic configuration of the computational domain with the complex terrain and actuator disk at the hilltop.

The complex terrain simulations are performed for a total time of $T_{ct} = 75s \approx 57 L_y/u*$, and the statistics are collected over the last $50s$. Results are presented for two different discretisation levels, hereafter referred to as low- and high-resolution simulations. The low-resolution mesh $(n_x \times n_y \times n_z = 193 \times 97 \times 64)$ has around 1M mesh nodes and is run for a total of $750,000$ time steps. Using 1024 cores, each low-resolution simulation takes 2h to finish. The high-resolution simulations double the resolution in each direction $(n_x \times n_y \times n_z = 385 \times 193 \times 128)$, which results in around 9.5M mesh nodes, and are run for $1,500,000$ time steps. Using 2048 cores, the wall clock time for each high-resolution simulation is around 12h. The ARCHER2 UK National Supercomputing Service with dual AMD EPYCTM 7742 64-core processors has been used to run these simulations.

3.1. Precursor simulation

The precursor simulation is a neutrally stable atmospheric boundary layer with the characteristics presented previously following the upstream flow conditions in Cao and Tamura [11]. The computational domain of the precursor simulation is $L_x \times L_y \times L_z = (3 \times 1 \times 1)\delta$. The precursor simulations are run for $T_p = 100s \approx 77 L_y/u*$, and the outflow planes and statistics are collected over the last $50s$.

The quality of the precursor simulation is assessed with the statistics of velocity and stresses. As shown in Figure 2a, the horizontally- and time-averaged streamwise velocity profile is compared against the upstream boundary layer presented in the experimental study [11] and the log-law profile $\frac{\langle u \rangle}{u_*} = \frac{1}{\kappa} \ln \left(\frac{y}{y_0} \right)$. Both low- and high-resolution simulations are able to represent the log-law profile of the experiment. Due to the no-slip boundary condition in the wall, it can be observed that the log-law profile is recovered after the first 3 to 5 nodes off the wall. The higher-resolution simulation approaches the desired profile at a lower distance from the wall than the lower-resolution simulation.

When using a constant pressure gradient of u_*^2/δ, the total stresses of a horizontal stationary turbulent boundary layer should follow: $1 - \frac{y}{L_y}$. Figure 2b shows the horizontally- and time-averaged resolved stresses $-\langle u_x' u_y' \rangle$ obtained for the ABL simulation with `WInc3D` for the two levels of resolution. It can be seen that the normalised resolved stresses follow the total theoretical

stress extending almost all the way down to the wall. As expected, the high-resolution simulation resolves better the near wall, but only marginally.

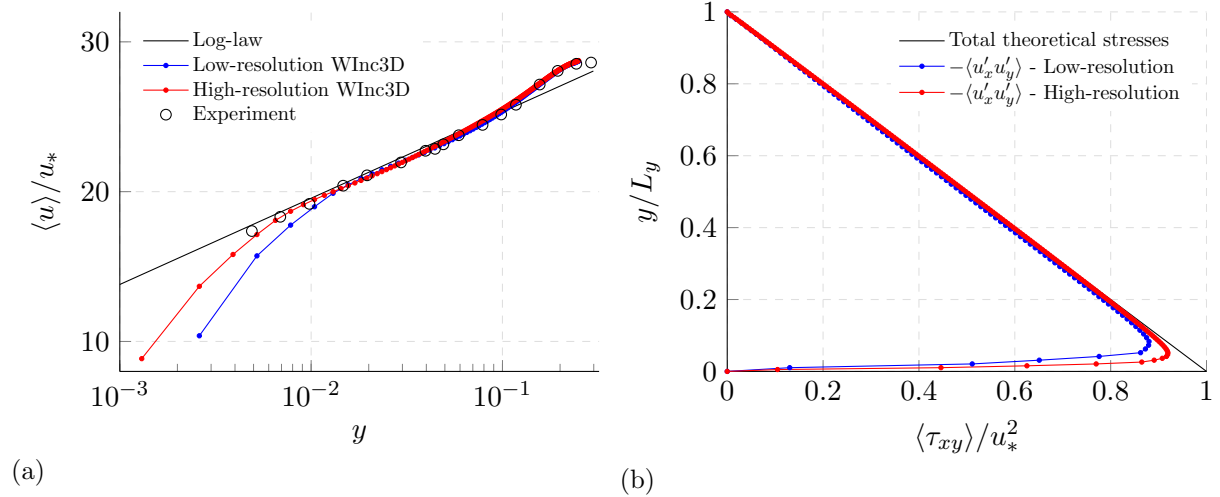(a)   (b)

Figure 2: Horizontally- and time-averaged streamwise velocity (a) and resolved stress profiles (b) of the simulated ABL compared against analytical profiles of a turbulent boundary layer and experimental data [11].

3.2. Complex terrain

In the experimental campaigns of Cao and Tamura [11], the measurements of the streamwise mean velocity and its variance were taken at different locations: $x/h = -2.5, -1.25, 0.0, 1.25, 2.5, 3.75, 5, 6.25, 7.5$. Figure 3a shows the time-averaged streamwise velocity $\langle u \rangle$ colour map obtained with the high-resolution simulation, as well as the time-averaged streamwise velocity profiles obtained from the two levels of resolution compared against the experiments, all normalised by the free stream velocity U_∞ sampled at $L_z = \delta/2$. It can be seen that both low- and high-resolution simulations get an excellent agreement with the experimental data at all the streamwise locations. From the colour map, it is possible to observe the different features of the flow around the hill. In front of the hill, the light red area indicates a zone with reduced velocity due to the blockage of the hill. We can also observe the acceleration of the flow on the windward side of the hill due to the favourable pressure gradient and that, after the peak, the flow separates. The white line represents the edge of the recirculation region that has been obtained with the contour of zero velocity to identify the edge of reverse flow. In both low- and high-resolution simulations, the flow reattaches around $x/h = 5.4$, which is within a 2.5% of error compared to the $x/h \approx 5.54$ reported by Cao and Tamura [11].

Figure 3b shows the time-averaged streamwise turbulence intensity σ_u colour map obtained with the high-resolution simulation normalised by U_∞, as well as the profiles obtained from the two levels of resolution compared against the experiments, normalised by $U_\infty/5$. Contrary to the streamwise velocity plots, differences between the two levels of resolution can be noted. The high-resolution simulation broadly agrees with the experiments while the low-resolution simulation displays larger errors in the near wake of the hill. The predictions of the two simulations are again in agreement after approximately $x/h = 5.0$. From the colour map, it can be seen that the detachment of the flow in the crest induces high turbulence levels downstream of it.
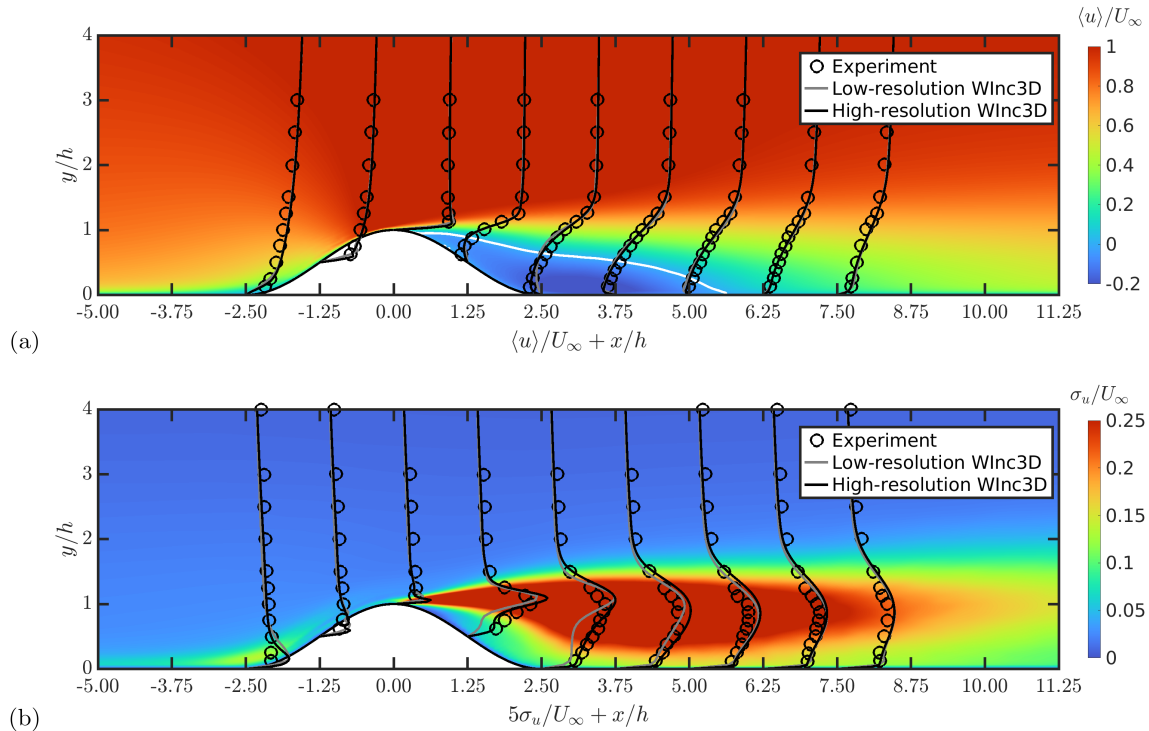
(a)

(b)

Figure 3: Code-to-experiment comparison between `WInc3D` and Cao and Tamura [11] for the normalised time-averaged streamwise velocity (a) and the normalised time-averaged streamwise turbulence intensity (b).

3.3. Wind turbine power

In this section, we use the same set-up as in the complex terrain simulations and account for the presence of the wind turbine with the ADM. To quantify the effect of the hill on the wind turbine's performance, the power of each wind turbine is normalised by the power generated by a wind turbine in flat terrain. If the normalised power is larger than one, the wind turbine takes advantage of the hill to produce more power.

Figure 4 shows the normalised power of a single wind turbine at different streamwise locations simulated with `WInc3D` using the low and high-resolution meshes. In the same plot, data from Zhang *et al.* [10] and Liu and Stevens [9] is included to compare against other computational studies that used the same set-up. The two levels of resolution give very similar results in terms of power output, except for $x/D = 1.25$ and 5, where some small discrepancies can be seen. `WInc3D` shows the same trends overall compared to the other studies; only small local differences can be seen. Data from Zhang *et al.* [10] agrees in all locations except at the top of the hill $x/D = 0$, where we see the larger difference. In general, Liu and Stevens [9] predict a higher power output compared to `WInc3D`. It has to be noted that this disagreement might arise from using a different actuator disk implementation. From the power distribution across the streamwise location, it can be seen that the power is not symmetrical to the hill and that three different regions can be identified; in front, on top and behind the hill. The blockage produced by the hill results in a reduction of power for the turbines located in front. Those located on top of the hill take advantage of the speedup and produce more power. Due to the flow separation in the leeward of the hill, wind turbines located after the hill produce much less power.
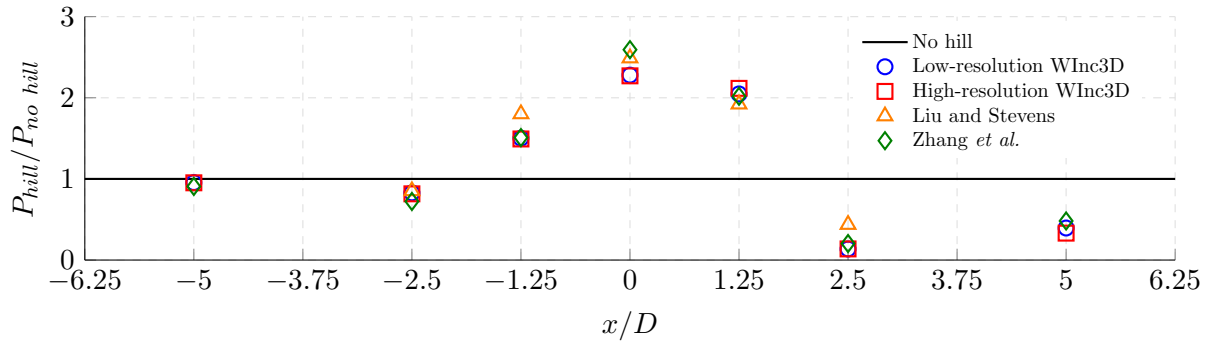
Figure 4: Normalised power output of a single wind turbine placed at different locations around the hill obtained with `WInc3D` and compared against other numerical studies [9, 10].

4. Results and discussion

We focus now on the three cases where $x/D = 0.0, 2.5$ and 5.0. The normalised time-averaged streamwise velocity field $\langle u \rangle / U_\infty$ for each case is shown in Figure 5 with the velocity profiles at different streamwise locations with and without the wind turbine using the high-resolution mesh. The recirculation region of the hill is also shown to see the changes produced by the wind turbine. The wind turbine at $x/D = 2.5$ is heavily affected by the reverse flow, which explains the much lower power output reported in Figure 4. Placing the wind turbine at $x/D = 5.0$ is not far enough to avoid the hill-wake negative effects. On the other hand, one can notice that the wind turbine on top of the hill, $x/D = 0.0$, generates an accelerated flow along the streamwise direction from the ground to the lower edge of the wind turbine's wake and reduces the hill recirculation zone. The improved conditions downstream of the turbine placed at the hilltop shows potential to improve the performance of wind turbines immersed in the hill wake.

The same methodology has been followed to investigate the wake-to-wake interaction for two cases where two wind turbines are placed around the hill, one on top of the hill and the other one at two locations, $x/D = 2.5$ and 5. One of the most interesting results is that the power output of the wind turbine placed at $x/D = 2.5$ is increased by a factor of 3 with respect to the result in Figure 4, where the upstream turbine was not present. Figure 6a shows how the downstream turbine takes advantage of the flow acceleration generated by the hill and hilltop wind turbine and the fact that the recirculation zone is reduced. However, the wind turbine at $x/D = 5.0$ does not improve its performance regardless of this acceleration on the near-wall flow; only an increase of 0.8% of power is accomplished. In this case, the velocity deficit produced by the upstream wind turbine is counteracting the improved conditions near the wall. This is shown in Figure 6b, specifically, in the profiles at $x/D = 3.75$, where a faster velocity can be seen on the bottom and a slower velocity on top compared to the case with no hilltop turbine.

As seen in Figure 3b, the hill induces high levels of turbulence due to the separation of the flow. The turbulence intensity, apart from influencing the wake recovery, is also affecting the turbine loading and power signal. Figure 7 shows the normalised time-averaged streamwise turbulence intensity for the cases with two wind turbines. To assess the changes produced by the upstream turbine, the profiles at different streamwise locations are included when the hilltop turbine is present and when it is not. When the downstream wind turbine is placed at $x/D = 2.5$, it seems to be experiencing the same levels of turbulence with and without the presence of the hilltop wind turbine. However, when placed at $x/D = 5.0$, a reduction in turbulence intensity is noticeable upstream of the wind turbine. This reduction is caused by the reduction of the recirculation zone produced by the hilltop wind turbine, as noted in Figure 5c. In both cases, it can be noted that the downstream turbulence intensity, e.g. $x/D = 7.5$, is reasonably reduced, leaving a cleaner condition for further rows of wind turbines.
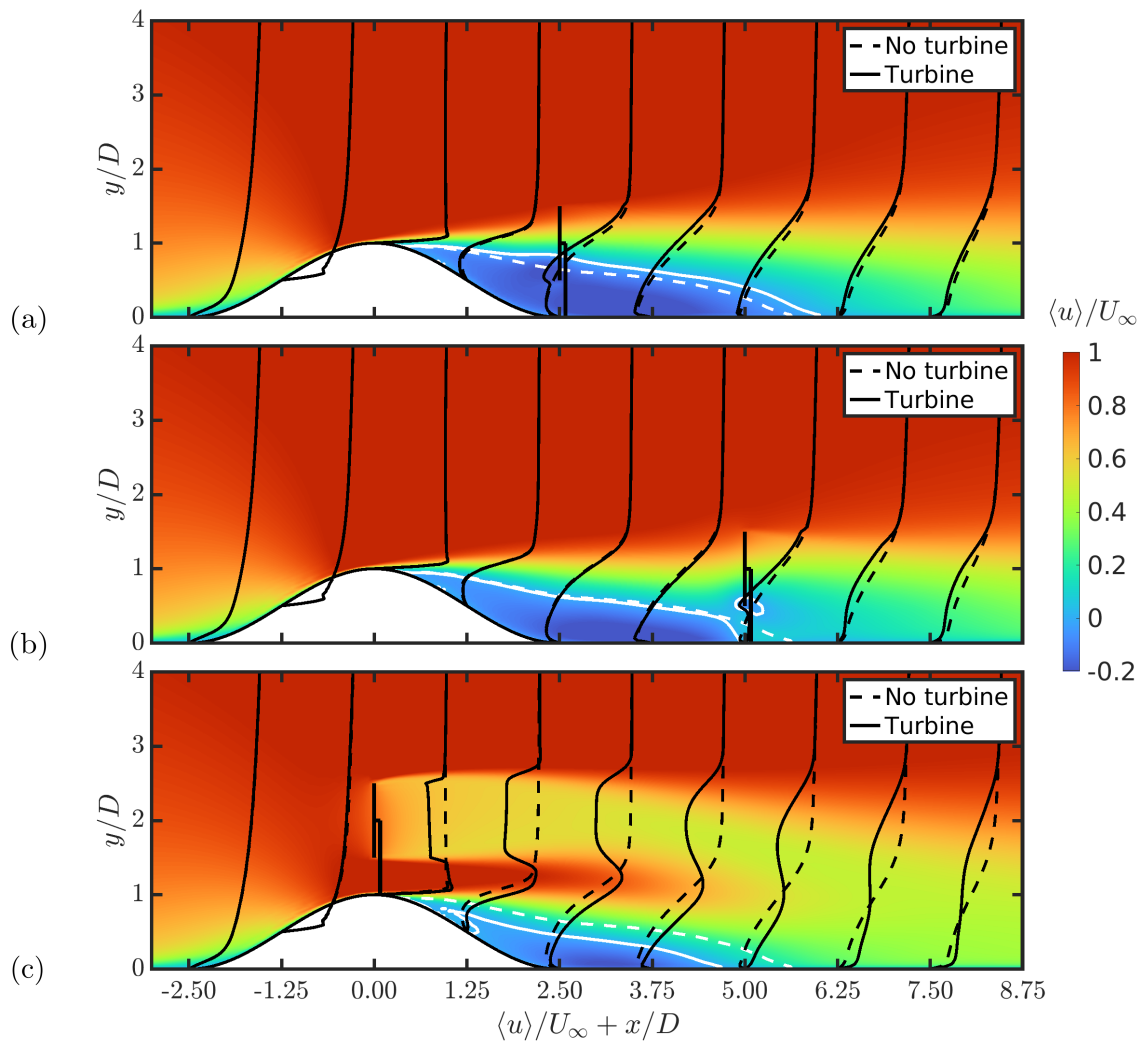
Figure 5: Normalised time-averaged streamwise velocity field with velocity profiles at different streamwise locations with and without the wind turbine.

5. Conclusions

In this work, we have validated an extension of the wind farm simulator `WInc3D` to perform LES of wind turbines in complex terrain by comparing results with previously published experimental and numerical data. Combing the IBM of Gautier *et al.* [22] with wall modelling has proven to be suitable for studying the interaction of the ABL with a hill, making `WInc3D` a good candidate for studying wind turbines in complex terrain, and still take advantage of its excellent scalability and high-order schemes features.

The code has been used to study the wake-to-wake interaction between two turbines influenced by the atmospheric boundary layer and a hill. It has been found that placing a wind turbine on top of the hill improves the performance of a downstream wind turbine; it reduces the recirculation zone of the hill wake and accelerates the flow near the wall. A wind turbine placed at 2.5D downstream of the hilltop is able to improve its performance by a factor of three when compared to the case with no turbine on the hilltop. If the downstream turbine is located at 5D from the top of the hill, there is no noticeable improvement in power production. These findings show the importance of understanding the flow field around complex terrain
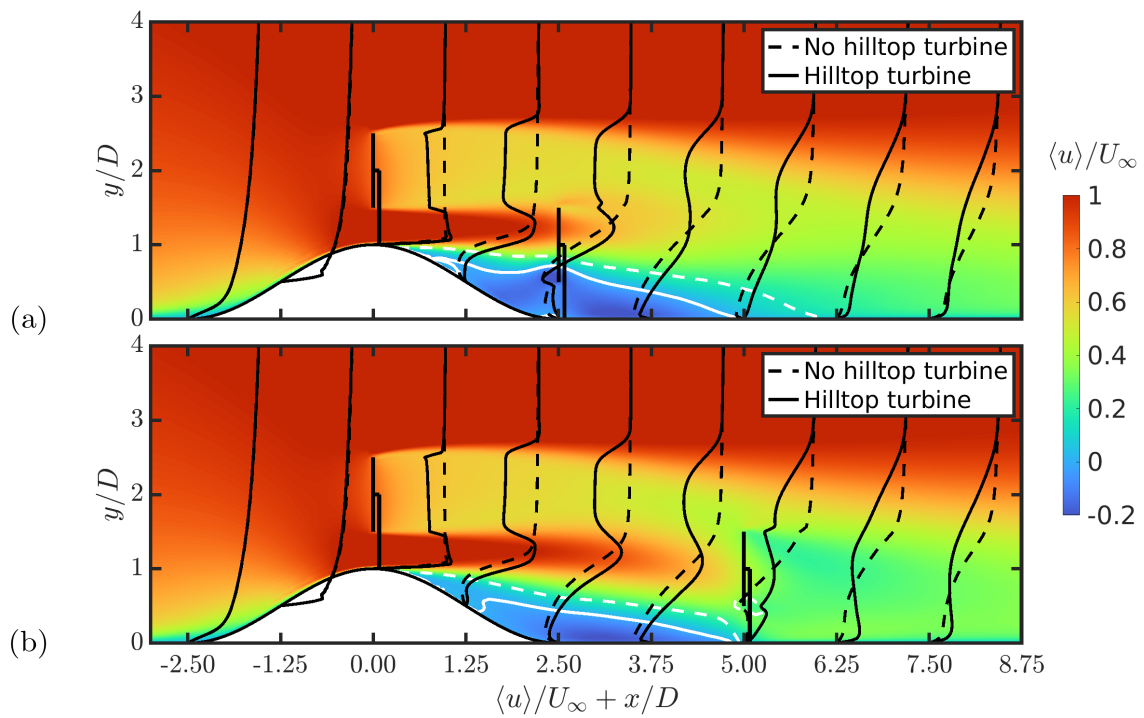
Figure 6: Normalised time-averaged streamwise velocity field with velocity profiles at different streamwise locations with and without the wind turbine on the hilltop.
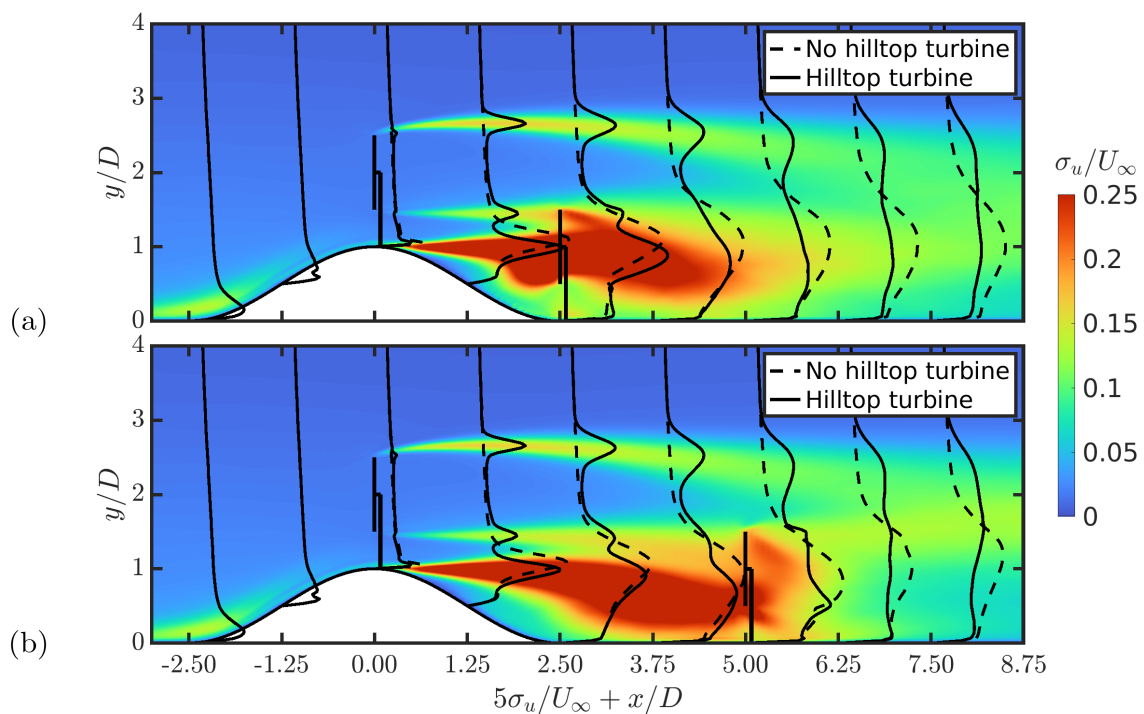

Figure 7: Normalised time-averaged streamwise turbulence intensity with profiles at different streamwise locations with and without the wind turbine on the hilltop.

when deciding the layout of a wind farm. The different enhancements of power seen for the two different locations suggest that there is an optimal downstream position where the maximum power increment can be obtained. In future work, it is planned to do a Bayesian Optimisation to find the streamwise location where the maximum power output from two turbines is obtained. Other sensible parameters that might improve the performance and further exploit the improved conditions downstream to the hilltop turbine, such as the hub height, will be included to find the best two-turbine set-up. Additionally, the findings of the study could be further validated by testing the optimal case with more accurate and more computationally expensive wind turbine parametrisation. Moreover, in order to improve the turbine modeling and capture the near wake dynamics and far wake meandering more accurately, it is suggested to consider the nacelle and tower, as recommended in the literature. Such upgrades to the turbine modeling could also help identify the limitations of the ADM in wind farms around complex terrain.

Acknowledgments

References

[1] Veers P *et al.* 2019 *Science* **366** eaau2027
[2] Veers P *et al.* 2022 *Wind Energ. Sci.* **7** 2491–6
[3] Stevens R J A M and Meneveau C 2017 *Annu. Rev. Fluid Mech.* **49** 311–39
[4] Porté-Agel F, Bastankhah M and Shamsoddin S 2020 *Boundary-Layer Meteorol.* **174** 1–59
[5] Yang X, Howard K B, Guala M and Sotiropoulos F 2015 *Phys. Fluids* **27** 025103
[6] Howard K B, Chamorro L P and Guala M 2013 *51st AIAA Aerospace Sciences Meeting including the New Horizons Forum and Aerospace Exposition 2013*
[7] Shamsoddin S and Porté-Agel F 2017 *Boundary-Layer Meteorol.* **163** 1–17
[8] Tian W, Ozbay A, Yuan W, Sarakar P and Hu H 2013 *51st AIAA Aerospace Sciences Meeting including the New Horizons Forum and Aerospace Exposition 2013*
[9] Liu L and Stevens R J A M 2020 *Boundary-Layer Meteorol.* **176** 251–69
[10] Zhang Z, Huang P, Bitsuamlak G and Cao S 2022 *Phys. Fluids* **34** 065123
[11] Cao S and Tamura T 2006 *J. Wind Eng. Ind. Aerodyn.* **94**(1) 1–19
[12] Deskos G, Laizet S and Palacios R 2020 *Wind Energ.* **23**(3) 779–94
[13] Bartholomew P, Deskos G, Frantz R A, Schuch F N, Lamballais E and Laizet S 2020 *SoftwareX* **12** 100550
[14] Smagorinsky J 1963 *Monthly Weather Review* **91** 99–164
[15] Calaf M, Meneveau C and Meyers J 2010 *Phys. Fluids* **22** 015110
[16] Meyers J and Meneveau C 2012 *Wind Energ.* **15** 305–17
[17] Goit J and Meyers J 2015 *J. Fluid Mech.* **768** 5–50
[18] Mason P J and Thomson D J 1992 *J. Fluid Mech.* **242** 51–78
[19] Laizet S and Lamballais E 2009 *J. Comput. Phys.* **228**(16) 5989–6015
[20] Lele S K 1992 *J. Comput. Phys.* **103** 16–42
[21] Laizet S and Li N 2011 *Int. J. Numer. Methods Fluids* **67**(11) 1735–57
[22] Gautier R, Laizet S and Lamballais E 2014 *Int. J. Comput. Fluid Dyn.* **28** 393–410
[23] Dairay T, Lamballais E and Benhamadouche S 2018 *Flow Turbul. Combust.* **100** 617–26
[24] Lamballais E, Vicente Cruz R and Perrin R 2021 *J. Comput. Phys.* **431** 110–5
[25] Wu Y T and Porté-Agel F 2011 *Boundary-Layer Meteorology* **138** 345–366
[26] Wu Y T and Porté-Agel F 2013 *Boundary-Layer Meteorology* **146** 181–205
[27] Yang X, Sotiropoulos F, Conzemius R J, Wachtler J N and Strong M B 2014 *Wind Energy* **18** 2025–2045
[28] Stevens R J, Martínez-Tossas L A and Meneveau C 2018 *Renewable Energy* **116** 470–478
[29] Li Z, Liu X and Yang X 2022 *Energies* **15** 6533 ISSN 1996-1073